Current Applied Science and Technology e-ISSN: 2586-9396

Curr. Appl. Sci. Technol. 2025, Vol. 25 (No. 5), e0262911

Research article

Intermediates Directing ZnO Nanoparticle Morphology for Enhanced Environmental Applications

Supasin Limsapapkasiphon[1], Weekit Sirisaksoontorn[2], Thammanoon Thaweechai[3], Apisit Songsasen[2] and Pannaree Srinoi[1]*

[1]Department of Chemistry, Faculty of Science, Kasetsart University, Bangkok, Thailand
[2]Department of Chemistry and Center of Excellence for Innovation in Chemistry, Faculty of Science, Kasetsart University, Bangkok, Thailand
[3]School of Integrated Science, Kasetsart University, Bangkok, Thailand

Received: 11 April 2024, Revised: 20 June 2024, Accepted: 20 November 2024, Published: 28 March 2025

Abstract

ZnO nanoparticles with adjustable morphology were synthesized using a variety of basic solutions. The formation of distinct intermediates during the synthesis process resulted in variations in the crystal structure, size, shape, and optical characteristics of the ZnO nanoparticles. In this study, ZnO nanoparticles were prepared via a simple precipitation method. The various ZnO intermediates formed with different basic solutions were identified using Fourier transform infrared spectroscopy (FTIR) and X-ray diffractometer (XRD). After calcination at 600°C, the XRD patterns revealed that all the ZnO nanoparticles produced were hexagonal wurtzite. However, the morphology of each ZnO synthesized varied due to the different intermediate formations and hydroxide ion concentrations present in the various basic solutions. Additionally, the photocatalytic performances of the synthesized ZnO variants were evaluated by the photodegradation of various organic dyes under UV irradiation. The results indicated that ZnO nanoparticles prepared with $NaHCO_3$ exhibited the highest photocatalytic efficiency.

Keywords: ZnO; nanoparticles; precipitation; synthetic mechanisms; photocatalyst

1. Introduction

Water is an important factor for living things such as humans, animals, and plants. Freshwater supplies are depleting due to increased population, industry, and untreated wastewater mixing with water resources, which is one of the key concerns confronting the world today (Tian et al., 2009; Benhebal et al., 2014; Nezamzadeh-Ejhieh & Khorsandi, 2014; Al-Tohamy et al., 2022). Wastewater containing organic pollutants, including dyes widely used in textiles, paints, leather, cosmetics, and food industries (Gnanaprakasam, 2015; Nguyen & Saleh, 2020), may greatly influence the quality of water and aquatic organisms. Therefore, complete treatment of wastewater is necessary. Water treatment procedures such as adsorption on clay, chemical precipitation, pollution separation,

*Corresponding author: E-mail: pannaree.sr@ku.th
https://doi.org/10.55003/cast.2025.262911

electrocoagulation, and other chemical and physical processes are employed to eliminate organic pollutants from wastewater (Nageeb, 2013; Tijani et al., 2014; Karpińska & Kotowska, 2019; Selvaraj et al., 2019). However, the major issue with these methods is that pollutants are not completely degraded but only transferred from one phase to another. Alternatively, the photocatalytic route has been considered an efficient method due to its eco-friendly properties resulting from the utilization of natural sunlight, its efficiency, and its cost-effectiveness when used for removing organic pollutants from wastewater (Rajamanickam & Shanthi, 2016; Razavi-Khosroshahi et al., 2017; Alanazi et al., 2021; Ferreira et al., 2021; Bao et al., 2021).

According to several studies, ZnO-based materials can be employed as a photocatalyst for the degradation of organic pollutants (Jiang et al., 2008; Ahmad et al., 2022; Bashir et al., 2022; Sansenya et al., 2022). ZnO in groups II–VI has a direct band gap of 3.37 eV and a large binding energy of ~60 meV at room temperature (Wittawat et al., 2020; Shi et al., 2021; Sharma et al., 2022). Furthermore, ZnO is a nanomaterial with excellent optical properties, high redox potential, good electron mobility, and is non-toxic. Due to these characteristic properties, it has been demonstrated to have potential applications in photocatalysis. As a photocatalyst, zinc oxide (ZnO) has several distinct advantages over other materials. One of its primary benefits is its wide bandgap, which allows it to effectively utilize ultraviolet (UV) light for photocatalytic reactions, making it highly efficient at degrading organic pollutants and disinfecting water. ZnO also has a high exciton binding energy, which enhances its photocatalytic performance by reducing recombination rates of electron-hole pairs, thereby improving the generation of reactive oxygen species essential for catalytic processes. Compared to titanium dioxide (TiO_2), another popular photocatalyst, ZnO offers higher electron mobility, which can lead to faster and more efficient charge transfer processes. This results in better performance in applications like environmental remediation and hydrogen production. ZnO nanoparticles could be synthesized by various methods, such as precipitation, sol-gel, hydro/solvothermal, combustion, electrochemical deposition, spray pyrolysis, and ultrasonic radiation (Kołodziejczak-Radzimska & Jesionowski, 2014; Ong et al., 2018; Weldegebrieal, 2020). After exploring various ZnO nanoparticle synthesis methods, the precipitation method stood out for its cost-effectiveness and simplicity, making it particularly advantageous for large-scale industrial applications and routine laboratory procedures (Shen et al., 1997; Lee et al., 2010; Sudha & Rajarajan, 2013). Additionally, its straightforward nature aligns with green methodologies, minimizing the need for hazardous chemicals. Overall, the precipitation method has proved to be a versatile, cost-effective, and environmentally friendly approach for ZnO nanoparticle synthesis. Many studies have found that the synthesis method of ZnO had a significant impact on its specific properties and applications (Xu et al., 2000; Hu et al., 2004; Kumar et al., 2013). In fact, several parameters in the synthesis process, such as aging time, pH, precursor concentration, reaction temperature, and calcination temperature, can influence the characteristics of the synthesized ZnO nanoparticles (Ismail et al., 2005; He et al., 2018; Abdulrahman et al., 2021; Arellano-Cortaza et al., 2021; Dey et al., 2021; Limón-Rocha et al., 2022).

The morphology of photocatalysts including size, shape, surface area, and crystallinity, plays a significant role in the photodegradation performance of photocatalysts. Normally, photocatalytic degradation involves several steps, including adsorption-desorption, electron-hole pair production, electron-hole pair recombination, and chemical reaction. The efficiency of each step is determined by the properties of the catalyst. Researchers are devoted to understanding how the photodegradation performance of ZnO is dependent on its structure. Controlling the size and form of ZnO nanostructures is essential for water treatment applications. Consequently, many studies have been carried

out to investigate the effects of size and shape on photodegradation efficiency. Several studies have focused on the synthesis route and various parameters such as pH, precursor, or temperature of ZnO synthesis, but only a few articles have addressed the effect of different bases on the properties of ZnO nanoparticles. The anisotropic growth habit of ZnO nanoparticles is greatly affected by external conditions such as temperature, solvent, precursor species, capping agents, and pH solution. It is well known that the morphology of synthesized ZnO strongly depends on the amount of hydroxide ions in the solution, which effectively determines particle nucleation, growth, and ripening (Moghri Moazzen et al., 2013; Tinio et al., 2015). Wahab et al. (2009) reported that the morphology of ZnO varied markedly from plate-like to rod-like structure when the pH value was increased from 6 to 12. Therefore, the characteristics and morphology of ZnO nanostructures could be controlled by fine-tuning the pH values of the reaction. Interestingly, the morphology of ZnO can be affected by variations in the intermediates that result from the use of different basic solutions. Specifically, each base has a different dissociation constant (K_b) that controls the pH of the solution, and the hydroxide precursor has a direct impact on the formation of intermediates and ZnO nanoparticles. However, the effects of the types of bases on intermediate formation was rarely discussed.

The aim of this work is to investigate the role of different base types and formation intermediates on the morphology and optical properties of ZnO nanoparticles. The as-prepared ZnO nanoparticles were synthesized using different basic solutions, including NaOH, KOH, NH_4OH, and $NaHCO_3$, via a simple precipitation method. Furthermore, the structure of ZnO intermediates before the calcination process was identified using Fourier transform infrared spectroscopy (FTIR) and X-ray diffraction (XRD). The ZnO samples after the calcination process were analyzed using scanning electron microscopy (SEM), X-ray photoelectron spectroscopy (XPS), energy-dispersive X-ray spectroscopy (EDX), photoluminescence spectroscopy (PL), ultraviolet–visible diffuse reflectance spectroscopy (UV-vis DRS), and the Brunauer-Emmett-Teller method (BET) to investigate the effects of different intermediate formations on the morphology, surface defects, elemental chemical composition, crystallinity, lattice parameters, and optical properties of the produced ZnO nanostructures. The ZnO nanoparticles synthesized with various basic solutions were evaluated for the photodegradation of organic dyes to investigate the photocatalytic performance.

2. Materials and Methods

2.1 Materials

Zinc acetate dihydrate ($Zn(CH_3CO_2)_2{\cdot}2H_2O$) was purchased from Kemaus, Australia. Polyvinylpyrrolidone (PVP, K30) and p-benzoquinone (PBQ, $C_6H_4O_2$) were purchased from Sigma-Aldrich, USA. Ethanol (C_2H_6O, absolute grade), ammonium hydroxide (NH_4OH, 25%) and sodium hydroxide (NaOH), were obtained from Merck, Germany. Sodium oxalate (SO, NaC_2O_4) was obtained from DAEJUNG, Korea. Isopropanol (IPA, C_3H_8O) was purchased from J.T. Baker, USA. Potassium hydroxide (KOH) and sodium bicarbonate ($NaHCO_3$) were purchased from Univar, New Zealand, and CARLO ERBA reagents in Italy, respectively. All chemicals were used without further purification.

2.2 Synthesis of ZnO nanoparticles with different types of bases

ZnO nanoparticles were prepared via a precipitation method. In a typical synthesis of ZnO, zinc acetate dihydrate (3.0 g, 0.14 mol) and PVP (0.6 g, 0.17 mmol) were dissolved in 100 mL ethanol and 2 mL deionized water and stirred for 15 min. A 40 mL of 1 M selected basic solution was added dropwise into the reaction mixture to form the precipitate and was continuously stirred for 1 h. Then, the solution was heated at 60^{o}C in an oven for 24 h. The precipitate was washed with deionized water several times and dried in an oven at 120^{o}C for 1 h. Finally, the crystalline ZnO nanoparticles were obtained by calcination in air at 600^{o}C with a heating rate of 5^{o}C/min for 3 h. The ZnO nanoparticles were prepared from various bases including NaOH, KOH, NH_4OH, and $NaHCO_3$. The corresponding calcined samples were labeled as zNaOH, zKOH, zNH_4OH, and z$NaHCO_3$, respectively.

2.3 Photocatalytic activity

The photocatalytic degradation of organic dyes was investigated by monitoring the absorbance change of selected organic dyes including basic blue 41 (BB41), acid orange 7 (AO7), and methylene blue (MB) under UV light (254 nm) for 4 h. Before the photodegradation, the adsorption process was performed in the dark for 30 min with stirring condition to achieve homogeneity of the reacting mixture. During the photoreaction, 5 mL of sample was collected every 30 min, then centrifuged at 3,000 rpm for 10 min to separate photocatalysts out from the solution. The absorption spectra of all experiments were determined by double-beam UV-visible spectrometer (UV/VIS Lambda 365, PerkinElmer). The absorption spectra of dyes were collected in range of 200 to 600 nm with spectral bandwidth (SBW) of 1 nm and a scan rate of 10 nm s^{-1}. Degradation efficiency was evaluated as follows:

$$\%\mathrm{D} = \frac{\mathrm{A}_0 - \mathrm{A}}{\mathrm{A}_0} \times 100\%$$

where A_0 and A represent the absorbance of dye solution before and after UV irradiation, respectively.

To study the photocatalytic mechanism, experiments were conducted to trap and identify the reactive radicals responsible for the degradation of BB41. These trapping experiments were conducted under conditions identical to those in the photodegradation experiments, with the introduction of specific scavengers to the suspensions before UV exposure. Three scavengers, namely, 10 mM isopropanol (IPA, C_3H_8O) for hydroxyl radicals ($^{\bullet}OH$), 10 mM sodium oxalate (SO, NaC_2O_4) for photo-induced holes (h^+), and 10 mM p-benzoquinone (PBQ, $C_6H_4O_2$) for superoxide radicals ($O_2^{-\bullet}$), were added to the reaction mixtures to capture and suppress the action of the investigated species during the photocatalytic reaction.

2.4 Characterization

X-ray diffraction (XRD) patterns were collected from 2 theta of 20 to 70 degree with a scan rate of 0.02^{o}s^{-1} on D8 Advance Bruker model with Cu Kα (1.5406 Å) used as an X-ray source. A scanning electron microscope or SEM (450 FEI model, Quanta) was used to determine the morphology and particle size of the catalyst. Before the measurements, all samples were coated by sputtering a thin layer of gold (Polaron Range SC7620 Sputter

Coater, Quorum Technology) to improve conductivity. Ultraviolet–visible diffuse reflectance spectra (UV–Vis DRS) were collected from wavelengths of 200 to 700 nm with spectral bandwidth (SBW) of 5 nm and a scan rate of 10 nm s^{-1} on PerkinElmer UV/VIS Lambda 365 spectrophotometer. Photoluminescence spectra (PL) were collected from wavelength of 200 to 800 nm with excitation and emission slit width of 10 nm and a scan rate of 10 nm s^{-1} on PerkinElmer LS55 with excitation wavelength of 325 nm. Attenuated total reflectance Fourier transform infrared spectroscopy or ATR-FTIR (Spectrum two, PerkinElmer) was used for the qualitative observation of molecular changes of the functional groups. The spectra were collected in the range between 400 and 4000 cm^{-1} with signal averaged over 16 scans at a resolution of 4 cm^{-1}. X-ray photoelectron spectroscopy (XPS) was performed using Kratos AXIS Ultra DLD spectrometer. The binding energies were calibrated by setting the C 1s peak at 284.8 eV as a reference. N_2 adsorption-desorption isotherm were collected with Micromeritics 3Flex Surface characterization at 77 K. The specific surface areas were estimated via the Brunauer-Emmett-Teller method (BET). The pore size and pore volume distributions were derived from the adsorption branches of the isotherms using the Barrett-Joyner-Halenda (BJH) model.

3. Results and Discussion

3.1 Synthesis and morphology of ZnO nanoparticles

To explore the impact of intermediate formation originating from diverse basic solutions, the formation process of ZnO was studied. Fourier transform infrared (FTIR) analysis emerged as a valuable technique for validating the composition of each ZnO intermediate. Figure 1 shows the FTIR spectrum of uncalcined ZnO prepared with different basic solutions. The proposed reactions corresponding to the formation of ZnO synthesized with different basic solutions are described in equations 1 to 9. Initially, the formation of ZnO occurs when Zn^{2+} and OH^- combine to form the white precipitate of $Zn(OH)_2$. In experiments with NaOH and KOH, a white precipitate formed immediately after a small amount of basic solution was added to the solution of Zn^{2+}. This rapid formation was due to the high dissociation of OH^- in strong bases, resulting in the rapid formation of zinc hydroxide ($Zn(OH)_2$) precipitates (equation 1). Additionally, $Zn(OH)_2$ is amphoteric, meaning it can react with both acids and bases. In the presence of an excess amount of a strong base, the initially formed $Zn(OH)_2$ precipitate can dissolve by forming a soluble complex ion, which is tetrahydroxozincate ion $[Zn(OH)_4]^{2-}$ (equation 2). This results in the disappearance of the white precipitate, as the $[Zn(OH)_4]^{2-}$complex ion is soluble in water. This behavior highlights the amphoteric nature of zinc hydroxide and the principles of solubility and complex ion formation. In this study, the FTIR pattern of zNaOH was similar to the zKOH pattern. The characteristic peaks observed at 548 and 888 cm^{-1} were attributed to the stretching and bending vibration modes of Zn-O and Zn-OH, respectively (Kołodziejczak-Radzimska et al., 2012; Park et al., 2014; Lamba et al., 2015). The presence of peaks around 1385, 1470, and 1640 cm^{-1} was related to the stretching vibration of the C-O and C=O groups of the zinc acetate precursor (Wahab et al., 2007; Lamba et al. 2017; Thongam et al., 2019). Thus, it was clear that $Zn(OH)_2$ was produced by the reaction of Zn^{2+} with strong bases (NaOH and KOH).

In the case of NH_4OH, the $Zn(OH)_2$ precipitate was dissolved and turned into a colorless $[Zn(NH_3)_4]^{2+}$ complex after the addition of concentrated NH_3 solution (equation 6-7), leading to the limited appearance of a white precipitate (Droepenu et al., 2020). When heated to 60^oC, the solution exhibited an increase in white precipitate, which resulted from

the slow reaction between the zinc amine complex and the OH^- in the solution. This reaction led to the formation of $[Zn(NH_3)_4](OH)_2$, which subsequently decomposed to ZnO (equations 8-9). From the FTIR spectrum, the peaks at 554, 905, 1391 and 1502, and 1645 cm^{-1} were assigned to the vibration of Zn-O, Zn-OH, C-O and C=O bonding, respectively. Additionally, the peaks at 835 and 1550 cm^{-1} were possibly related to N-H bonding from zinc amine complex, indicating that zinc amine hydroxide complex ($[Zn(NH_3)_4](OH)_2$) was obtained. Furthermore, when $NaHCO_3$ was used in the experiment, the dissociation of a weak base in water was described by equations 3-4. The rapid formation of insoluble complex, zinc hydroxy carbonate ($[ZnCO_3]_2 \cdot [Zn(OH)_2]_3$), was observed (equation 5). The FTIR spectrum of ZnO intermediate synthesized with $NaHCO_3$ was different from the other ZnO samples, with the peaks at 1045, 1378, and 1508 cm^{-1} which were related to the stretching vibration of CO_3^{2-}. There were two sharp peaks at 707 and 834 cm^{-1} corresponding to the O-C-O bending mode, and a band at 469 cm^{-1} attributed to the Zn-O vibration. This result also proved that the intermediate of ZnO nanoparticles prepared with $NaHCO_3$ was zinc hydroxy carbonate (Shamsipur et al., 2013; Lin et al., 2014). The absorption peak of all ZnO samples in the range of 3200-3400 cm^{-1} was ascribed to the stretching vibration of hydroxyl group and the peak around 2900 cm^{-1} was attributed to C-H stretching from acetate group and stabilizing agents.

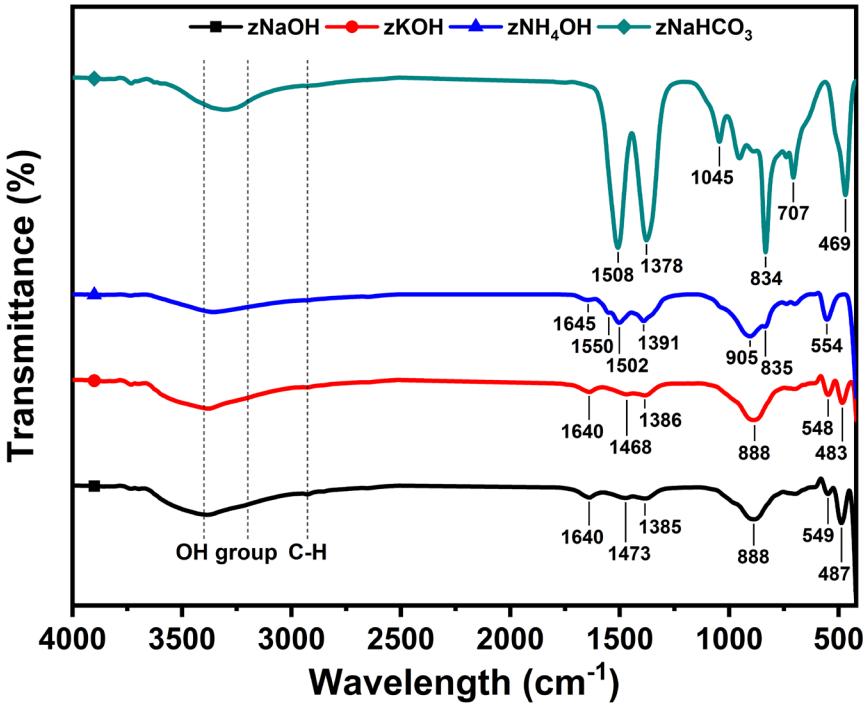

Figure 1. FTIR spectra of ZnO prepared with different types of bases before calcination process

ZnO synthesized with NaOH and KOH (zNaOH and zKOH)

$$Zn^{2+}_{(aq)} + 2OH^-_{(aq)} \rightleftharpoons \mathbf{Zn(OH)_2}_{(s)} \quad (1)$$

$$Zn^{2+}_{(aq)} + 4OH^-_{(aq)} \rightleftharpoons Zn(OH)_4^{2-}{}_{(aq)} \quad (2)$$

ZnO synthesized with $NaHCO_3$ ($zNaHCO_3$)

$$NaHCO_{3\,(s)} \longrightarrow Na^+_{(aq)} + HCO_3^-{}_{(aq)} \quad (3)$$

$$HCO_3^-{}_{(aq)} + H_2O_{(l)} \rightleftharpoons OH^-_{(aq)} + H_2CO_{3\,(aq)} \quad (4)$$

$$2Zn^{2+}_{(aq)} + 2OH^-_{(aq)} + 2H_2CO_{3\,(aq)} \longrightarrow \mathbf{[ZnCO_3]_2{\bullet}[Zn(OH)_2]_3}_{(s)} \quad (5)$$

ZnO synthesized with NH_4OH (z NH_4OH)

$$NH_{3\,(l)} + H_2O_{(l)} \rightleftharpoons NH_4^+{}_{(aq)} + OH^-_{(aq)} \quad (6)$$

$$Zn(OH)_{2\,(s)} + 4NH_{3\,(l)} \rightleftharpoons [Zn(NH_3)_4]^{2+}{}_{(aq)} \quad (7)$$

$$[Zn(NH_3)_4]^{2+}{}_{(aq)} + 2OH^-_{(aq)} + \text{heat} \longrightarrow [Zn(NH_3)_4](OH)_{2\,(aq)} \quad (8)$$

$$[Zn(NH_3)_4](OH)_{2\,(aq)} \longrightarrow \mathbf{ZnO}_{(s)} \quad (9)$$

The morphology and particle sizes of ZnO prepared with different basic solutions were determined by scanning electron microscope (SEM). The average particle sizes of all synthesized samples from SEM images are listed in Table 1. As shown in Figure 2, the sizes of zNaOH, zKOH, and $zNaHCO_3$ were homogeneous and slightly aggregated, forming agglomerates with particle sizes of 62, 64, and 165 nm, respectively. Furthermore, a flower-like morphology appeared in zNH_4OH, with particle sizes larger than 1000 nm. This finding seems to confirm the effect of the intermediate $[Zn(NH_3)_4](OH)_2$ formation on the synthesis of ZnO nanoparticles by influencing particle formation and morphological structure. The formation of the flower-like structure was attributed to the slow decomposition of the $[Zn(NH_3)_4](OH)_2$ intermediate. This process involves the gradual release of Zn^{2+} and OH^- ions upon heating, allowing for a controlled crystallization process. This controlled release leads to slow crystallization, with growth along the c-axis being particularly promoted by the influence of the dipole moments of the crystal planes. This growth in the c-axis direction significantly contributes to the development of flower-like structures. It was discovered that each base has various basic characteristics after determining the differences between strong bases, NaOH and KOH, and weak bases, NH_4OH and $NaHCO_3$. The base dissociation constant (K_b) is a parameter that influences the concentration of hydroxide ions in solution. Furthermore, the K_b value can be used to determine ZnO growth efficiency. In other words, high K_b values act as a strong reaction driving force, enhancing ZnO growth efficiency and resulting in tiny particle sizes. The dissociation constant of each base is given in Table 1.

Table 1. Particles size of ZnO samples and base dissociation constants of base precursors

Samples	Particles size (nm)	Base dissociation constant (K_b)	Morphology	Band gap (eV)
zNaOH	62	0.63	Spherical	2.99
zKOH	64	0.31	Spherical	2.97
zNH_4OH	>1000	$1.8x10^{-5}$	Flower-like	2.98
z$NaHCO_3$	165	$2.0x10^{-8}$	Spherical	3.13

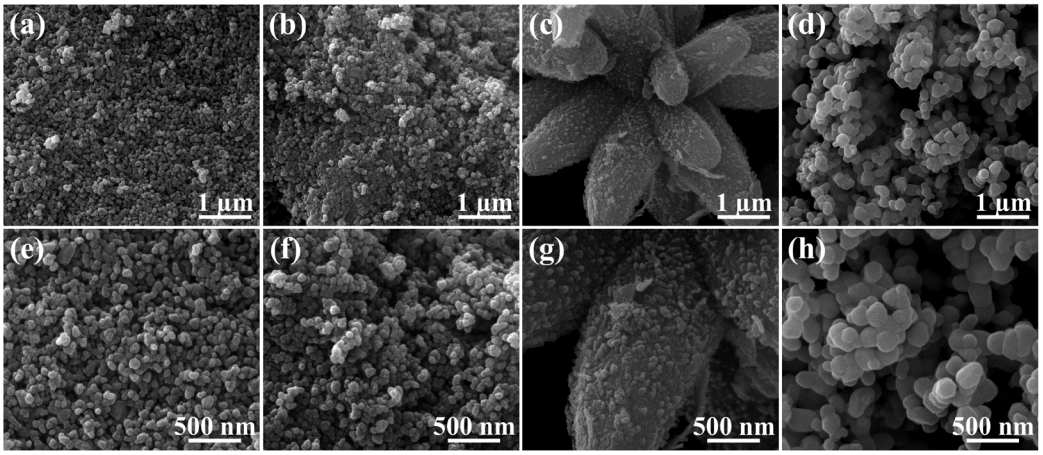

Figure 2. SEM images of ZnO samples synthesized with different bases: (a, e) zNaOH, (b, f) zKOH, (c, g) zNH_4OH, and (d, h) z$NaHCO_3$

The X-ray diffraction (XRD) patterns of all ZnO nanoparticles are shown in Figure 3. The diffraction peaks appeared at 2θ = 31.8°, 33.4°, 36.2°, 47.5°, 56.5°, 62.8°, 66.3°, 67.9°, and 69.0° corresponding to (100), (002), (101), (102), (110), (103), (200), (112), and (201) planes, indicating the formation of hexagonal wurtzite structure of ZnO (Ashraf et al., 2015; Sulciute et al., 2021). The sharp peaks observed indicate that the synthesized ZnO nanoparticles exhibited high crystallinity with a single phase of the wurtzite structure. The average crystallite size of the ZnO crystals were calculated from the Full Width Half Maximum (FWHM) of the diffraction peaks using the Debye–Scherrer equation (Benhebal et al., 2014;-Dhir, 2020). The average crystallite sizes of all synthesized ZnO samples from the calculated XRD pattern were listed (data not shown). The average crystallite sizes of zNaOH, zKOH, zNH_4OH, and z$NaHCO_3$ were determined to be 35.54, 33.42, 23.83, and 49.10 nm, respectively. The differences in crystallite size might be attributed to the varying values of the dissociation constants of the bases (K_b). Specifically, the K_b values of NaOH, KOH, NH_4OH, and $NaHCO_3$ were 0.63, 0.31, 1.8×10^{-5}, and 2.0×10^{-8}, respectively (Aracena et al. 2020; Eikeland et al., 2021; Remor et al., 2023). The rate of nucleation and growth of ZnO crystals was affected by the variation in K_b. The high K_b value of a strong base corresponds to a high concentration of OH^- in the basic solution, resulting in rapid nucleation of ZnO crystals and consequently smaller crystallite sizes.

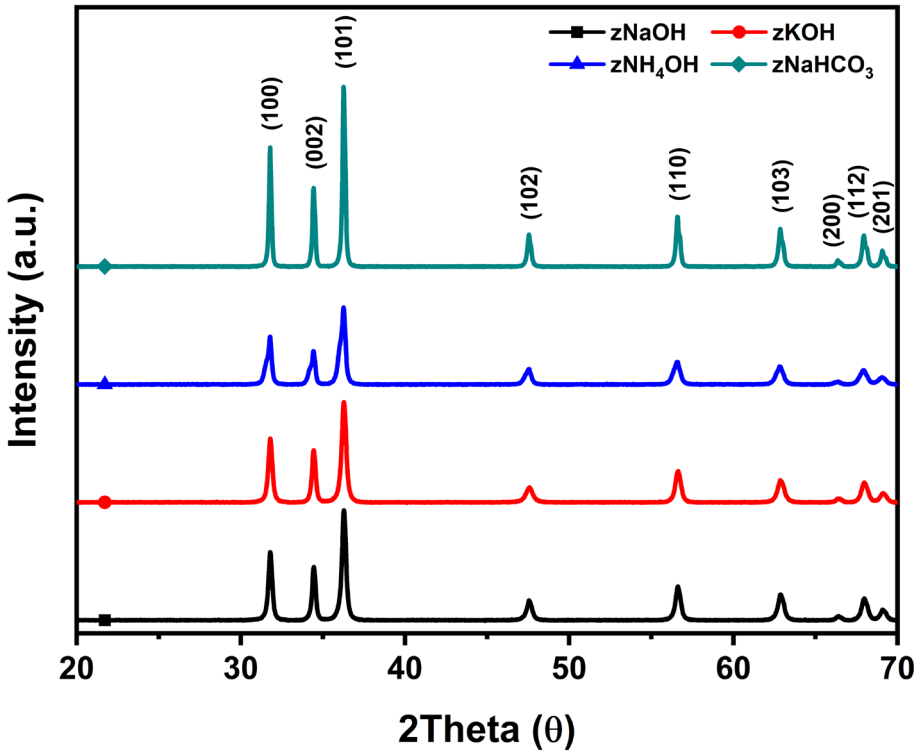

Figure 3. XRD patterns of all prepared ZnO samples after calcination at 600°C for 3 h

However, zNH_4OH showed the lowest average crystallite size despite the relatively low K_b value. This outcome can be attributed to the chemical reaction between $Zn(CH_3CO_2)_2$ and NH_4OH. Upon adding concentrated NH_3 solution to the mixture, a zinc amine complex is immediately formed. After heating at 60°C, the zinc amine complex slowly reacts with OH^- in the solution to form zinc amine hydroxide, which eventually decomposes and ZnO is formed. The increase in grain boundary in the structure might have led to a decrease in the crystallite size due to particle time-consumption growth. Based on the recorded XRD pattern, all synthesized ZnO samples exhibited wurtzite structures, characterized by a hexagonal crystal system (space group P63mc) (Wang et al., 2012). The XRD patterns were in good agreement with hexagonal wurtzite ZnO from JCPDS data No. 36-1451 (a = 0.3250 nm and c = 0.5202 nm) (Zegadi et al., 2014). Except for zNH_4OH, the lattice parameter along the c-axis was higher than that of other samples. However, the increased lattice parameter along the c-axis observed in zNH_4OH samples was probably due to distortions within the crystal structure caused by the formation of Zn metal, as described in the XPS section. In general, ZnO crystal structures are formed on two major crystal planes: the polar plane and the non-polar plane. The polar plane of the wurtzite crystal structure of ZnO consists of a positive (001) plane consisting of Zn lattice sites and a negative $(00\bar{1})$ plane consisting of oxygen lattice sites. This sequential arrangement of Zn^{2+} and O^{2-} results in the formation of a dipole moment and spontaneous polarization along the c-axis, as well as a variance in surface energy (Baruah & Dutta, 2009; Zou et al., 2022). Therefore, at lower concentrations, hydroxide ions could potentially be more stable on positive polar (001) planes than on other planes. The stability of

hydroxide ions on the (001) planes of ZnO crystals at lower concentrations stems from the favorable surface energy of these planes compared to others. With fewer hydroxide ions available in the solution, they preferentially adsorb onto these stable surfaces due to specific atomic arrangements that facilitate stronger interactions. This preference directs the crystal growth along the c-axis, perpendicular to the (001) planes, leading to the formation of the flower-like structures observed in Figure 2c. These structures emerge as successive layers of ZnO that accumulate outward from the central axis, reflecting the crystal's growth pattern driven by the stability of hydroxide ions on the (001) planes.

The micro-strain (ε) of the ZnO nanoparticles was calculated and the result are shown in Table 2. The micro-strain in ZnO structure originates from local distortions within the crystal lattice structure, which may result from factors such as impurities, defects, and mechanical stresses. These distortions can cause substantial changes in the properties of the material, including its mechanical strength, electrical conductivity, and optical behavior (Chithra et al., 2015). As shown in Table 2, the $zNaHCO_3$ showed the lowest value of micro-strain, which indicated that the defects in the crystal structure decreased in $zNaHCO_3$ structure. On the other hand, the increase in micro-strain of other ZnO nanoparticles may be due to the creation of lattice imperfections, which could be seen in the color appearance of the samples (McCluskey & Jokela, 2009). Additionally, the volume of the nanoparticles (v) and the Zn-O bond length (l) were calculated, as shown in Table 2 (Modwi et al., 2019). The calculated Zn-O bond length was found to be similar for all ZnO nanoparticles.

Table 2. Structure characteristics properties of ZnO prepared with different bases.

Samples	$V_{(101)}$ (nm^3)	v (nm^3)	ε (10^{-3})	l (Å)
zNaOH	13,772	0.0822	1.17	1.8845
zKOH	13,537	0.0822	1.17	1.8846
zNH_4OH	4,925	0.0827	1.64	1.8881
$zNaHCO_3$	48,255	0.0823	0.77	1.8850

V is the volume of the particle; ***v*** is the volume of the unit cell; ***ε*** is micro-strain; and ***l*** is bond length

The ZnO nanostructures described above were characterized by X-ray photoelectron spectroscopy (XPS) for the validation of their surface elemental composition. Figure 4a displays the typical XPS wide scan spectra of zNaOH, zKOH, zNH_4OH, and $zNaHCO_3$. Across all samples, characteristic peaks corresponding to Zn 2p, O 1s, and C 1s were observed throughout the entire region of the XPS spectra. The high resolution XPS of Zn 2p, O 1s, and C 1s of all ZnO samples are shown in Figure 4b, 4c, and 4d, respectively. The high-resolution signal of Zn 2p were split into two peaks at binding energy of about 1022 and 1045 eV, corresponding to spin orbit splitting of 23 eV between Zn $2p_{3/2}$ and Zn $2p_{1/2}$ for all samples. The peak positions and peak split were consistent with the oxidation state of Zn^{2+} in ZnO nanostructure (Rabin et al., 2016). The XPS spectrum of the O 1s region presented an asymmetric peak, indicating the presence of different oxygen species. Additionally, the high-resolution C 1s deconvoluted XPS spectra of all ZnO samples reveal various carbon species within the ZnO structures, originating from the use of zinc acetate as the Zn precursor.

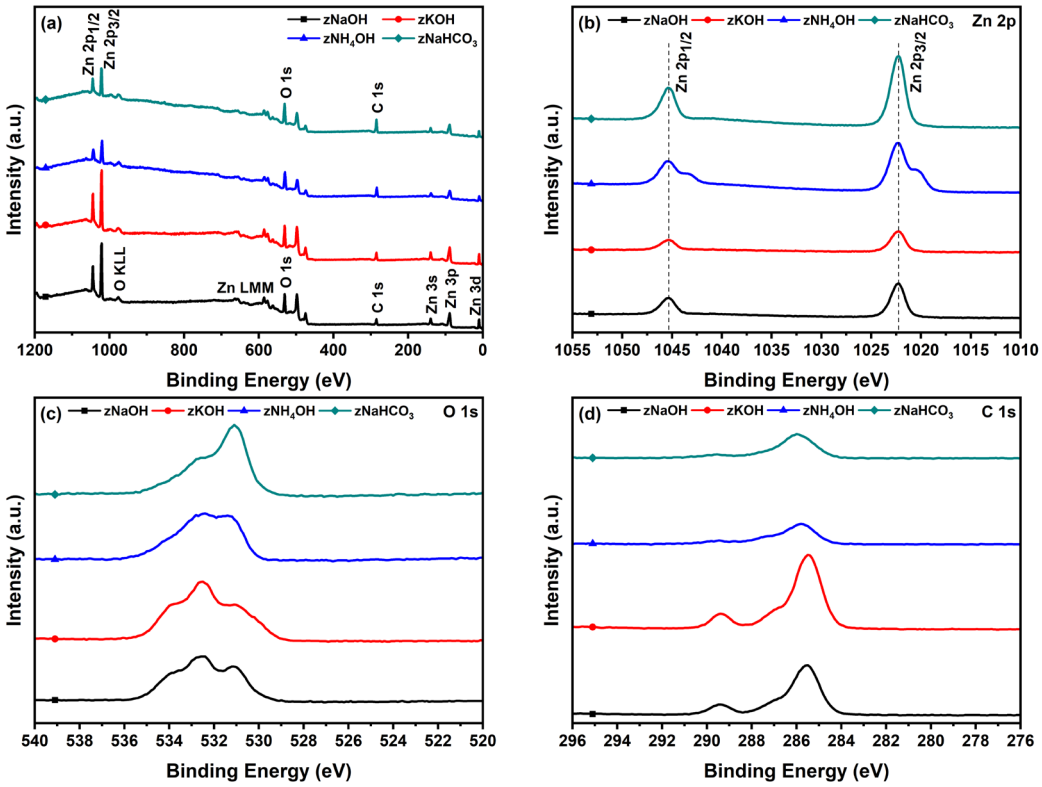

Figure 4. (a) XPS wide survey, (b) Zn 2p, (c) O 1s, and (d) C 1s spectra of ZnO prepared with different bases

The deconvolution of Zn $2p_{3/2}$ spectra of all samples are shown in Figure 5. The Zn $2p_{3/2}$ spectra of zNaOH, zKOH, $zNaHCO_3$ could be deconvoluted into two components at binding energies 1022 and 1023 eV, which were attributed to Zn^{2+} in ZnO and $Zn(OH)_2$, respectively (Kumar & Ahmad, 2020). Unlike XPS Zn $2p_{3/2}$ of zNaOH, zKOH, $zNaHCO_3$, the Zn $2p_{3/2}$ of zNH_4OH peak was deconvoluted into three components at binding energies of 1020, 1022, and 1023 eV which corresponded to Zn metal, ZnO, and $Zn(OH)_2$, respectively (Galmiz et al., 2015). It was possible that the phenomenon was caused by reduction of Zn^{2+} in zinc oxide structure to zinc metal during the calcination process (Auer et al., 2022). This unique outcome could be attributed to the role of the NH_4OH precursor in the synthesis process. The decomposition of $[Zn(NH_3)_4]^{2+}$ occurrs at low temperatures and involves rapid kinetic transformation into ZnO (Park et al., 2014)]. During this transformation, the release of NH_3 from the complex is likely trapped within the rapidly growing crystal lattice of ZnO. Subsequently, in the calcination process, this entrapped NH_3 undergoes thermal decomposition into hydrogen (H_2) and nitrogen (N_2) (Reli et al., 2015; Sun et al., 2018; Lucentini et al., 2021). This reaction is facilitated by ZnO, which acts as a support catalyst in this environment. Additionally, at elevated temperatures, the generated hydrogen (H_2) functions as a reducing agent, engaging in a reaction with ZnO (Lew et al., 1992; Sasaoka et al., 1994; Qi & Hu, 2020). This reduction process eliminates oxygen from ZnO, transforming it into its metallic state.

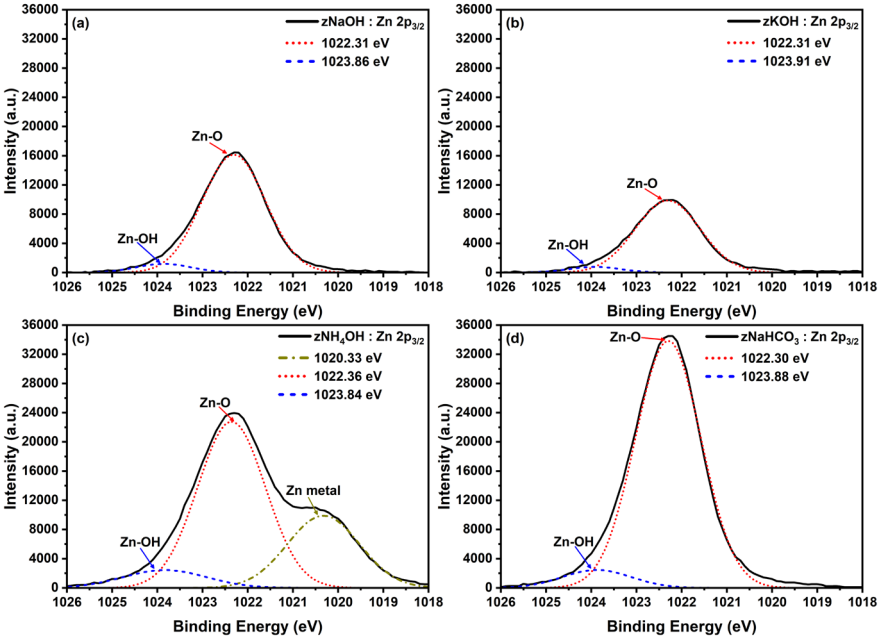

Figure 5. The high-resolution Zn $2p_{3/2}$ deconvoluted XPS spectra of (a) zNaOH, (b) zKOH, (c) NH_4OH, and (d) $zNaHCO_3$.

Furthermore, the XPS spectrum of O 1s was performed to understand the existence of different forms of oxygen bonding on their surface. The obtained results are shown in Figure 6. In all samples, the XPS O 1s exhibits three Gaussian peaks in deconvoluted spectra. The lattice oxygen was at 531 eV which corresponded to the O^{2-} in ZnO wurtzite structure. The other peaks at 533 and 534 eV were related to the OH^- group and C=O surface bonding absorbed on the surface of ZnO (Chandrappa & Venkatesha, 2012; Al-Gaashani et al., 2013; Claros et al., 2020). The amount of surface adsorption could be related to the role of surface defects of metal oxides, which corresponded to the intensity of the peak at 532 eV (Sahai & Goswami, 2014; Kwoka et al., 2020; Uribe-López et al., 2021). According to Figure 6, the highest intensity of O 1s at 532 eV was shown in zNH_4OH, followed by zKOH, zNaOH, and $zNaHCO_3$. This result indicated that zNH_4OH had more surface imperfections than zKOH, zNaOH, and $zNaHCO_3$, respectively. This observation seemed to be consistent with the crystallinity of ZnO samples, which was discussed in the previous section. An oxygen vacancy occurs when oxygen sites within the crystal lattice are left unoccupied during crystal growth, introducing imperfections and distortions in the crystal lattice structure (Sahu et al., 2022). Consequently, the presence of these defects leads to the expansion of grain boundaries within the crystal. These grain boundaries act as interfaces between adjacent crystallites, causing structural discontinuity and resulting in a reduction in the overall crystallite size (Liu et al., 2018). Furthermore, the presence of oxygen vacancies in ZnO introduces additional energy states within the band gap of ZnO (Chen et al., 2020). These energy states trap electrons, which then have the potential to interact with photons of light. This interaction leads to a phenomenon known as deep-level emission, which is often observed as a change in the color of ZnO (Sahai & Goswami, 2014).

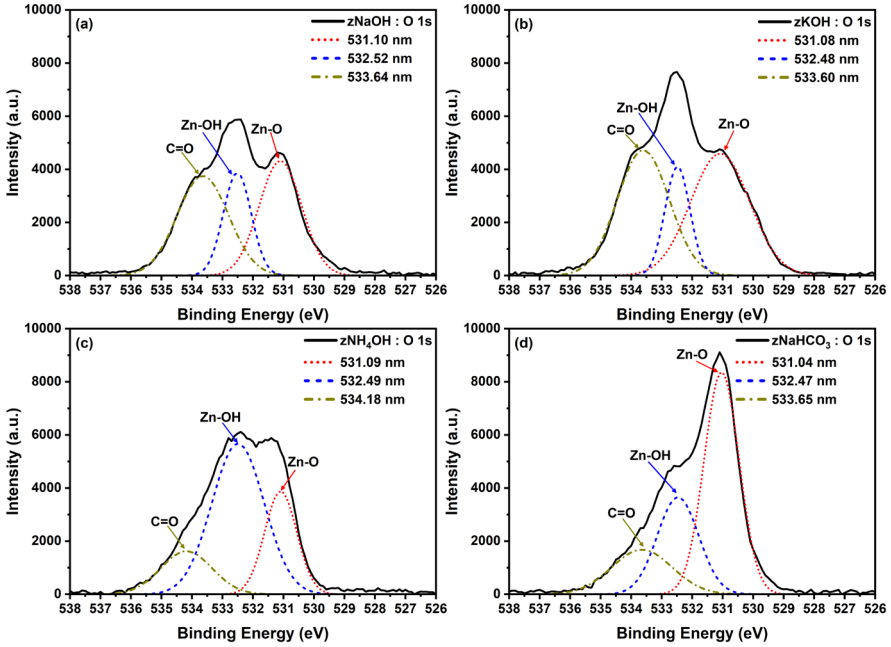

Figure 6. The high-resolution O 1s deconvoluted XPS spectra of (a) zNaOH, (b) zKOH, (c) NH_4OH, and (d) $zNaHCO_3$.

3.2 Optical properties of ZnO nanoparticles

The optical properties of ZnO nanoparticles were highly sensitive to structural defects, as evidenced by photoluminescence (PL) analysis. To investigate the impact of different precursors on the optical properties of ZnO, 5 mg of ZnO powder was dispersed in 10 mL distilled water, and the PL spectrum was recorded at room temperature with an excitation wavelength of 325 nm. As shown in Figure 7a, all the samples exhibit two distinct emission zones in the UV range (387-391 nm), referred to as near-band-edge emission (NBE), and a broad visible emission (DL) ranging from 402 to 590 nm. The PL intensity of a semiconductor is known to depend on the defect density within the structure (Chithra et al., 2015; Zhang et al., 2019). Compared to the other samples, $zNaHCO_3$ displayed a higher UV emission intensity due to the higher concentration of free excitons, which could be attributed to the better crystallinity of its nanoparticles (Wu et al., 2007; Raj & Sadayandi, 2016; Ayoub et al., 2022). In contrast, the lower UV emission intensity of zNH_4OH indicated a higher degree of structural defects in the nanoparticles, consistent with the micro-strain calculation findings obtained from the XRD analysis. Therefore, the increase in micro-strain led to a reduction in the crystallinity and photoluminescence intensity of ZnO nanoparticles.

The position of the emission peak remains consistent across all samples despite differences in synthesis methods. The only observable difference between the samples appears to be their color, which might be attributed to crystal defects or the incorporation of other elements into the crystal structure (Manzoor et al., 2009). However, no observable emissions related to the color of ZnO were detected in all samples. Figure 7b displays the UV-Vis DRS spectra of ZnO synthesized using different basic solutions. The band gap

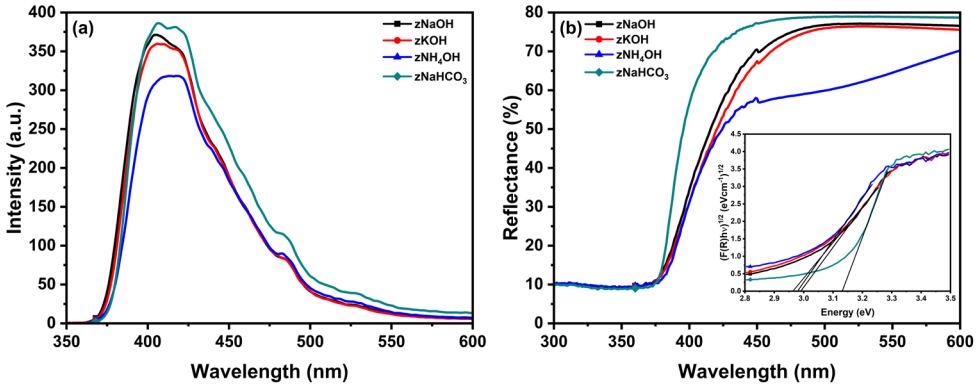

Figure 7. The PL spectra (a) and UV-vis DRS spectra (b) of ZnO prepared with different types of bases. Inset: The corresponding plots of $(F(R)hv)^{1/2}$ versus energy for the band gap energy of ZnO.

energy (E_g) of each sample was obtained by extrapolating $(F(R)\ hv)^{1/2}$ to hv, as shown in the inset. The band gap values obtained from the measurements are listed in Table 1. Among the samples, zNaOH, zKOH, and zNH_4OH had a small amount of absorption in the visible-light region, indicating that they were effective photocatalysts under visible light. Conversely, $zNaHCO_3$ only absorbed light in the wavelength region of less than 400 nm. The differences in color of ZnO samples provided clear indications of the different light absorption properties of the materials. The band gap energy was measured to be 2.99, 2.97, 2.98, and 3.13 eV for zNaOH, zKOH, zNH_4OH, and $zNaHCO_3$, respectively. This observation was different from the SEM experiment. Generally, the quantum size effect is most pronounced for semiconductor nanoparticles, where the band gap increases with decreasing particle size (Singh et al., 2018; Agarwal et al., 2019; Moussa et al., 2021). However, the band gap of zNaOH and zKOH samples, which had similar particle sizes, was found to be smaller than that of $zNaHCO_3$, indicating that the quantum confinement effect was not allowed in this case. In addition, doping of an element was one factor for tuning the band gap of a semiconductor (Das et al., 2013; Benhebal et al., 2014; Rahman et al., 2022). It is well known that dopants could introduce impurity levels within the band gap, which might lead to a reduction in the band gap energy of semiconductors (Bhattacharyya & Gedanken, 2008; Marinho et al., 2019). EDS analysis was carried out to detect impurity doping in the crystal structure of ZnO. The findings presented in Table 3 indicate that Na, K, and N impurities were detected in each of the ZnO nanostructures, suggesting that these impurity ions had been doped during the particle growth and aging process (Xu et al., 2008; Benhebal et al., 2014; Kumari et al., 2015; Erdogan et al., 2021). The incorporation of dopant elements into the ZnO structure can potentially reduce its band gap, leading to greater absorption of light in the visible region and resulting in a color change in the samples.

3.3 Physical properties of ZnO nanoparticles

The physical properties of various ZnO samples were determined using the Brunauer-Emmett-Teller (BET) method, which involved measuring N_2 adsorption-desorption

isotherms. The type-IV adsorption isotherms obtained for all samples, according to IUPAC classification, suggested that the samples had a mesoporous structure (McLaren et al., 2009; Kołodziejczak-Radzimska et al., 2012; Pandey et al., 2021). The adsorption-desorption isotherms for ZnO prepared with different types of bases were recorded. Table 3 summarizes the specific surface area (S_{BET}), pore volume, and average pore diameter of all samples. The calculated S_{BET} values were 14.10, 15.31, 6.11, and 5.26 m^2/g for samples zNaOH, zKOH, zNH_4OH, and z$NaHCO_3$, respectively. These results were consistent with the particle size of ZnO samples from the SEM technique, where particle sizes were typically inversely proportional to surface area. However, the zNH_4OH sample exhibited a decrease in specific surface area, which could be attributed to its flower-like morphology. Additionally, the average pore size of all samples increased with increasing S_{BET} and was less than 50 nm, indicating that the samples were mesoporous materials.

Table 3. Energy dispersive X-ray spectroscopy (EDS) results and specific surface area (S_{BET}), pore volume, and average pore diameter of ZnO prepared with different bases

Samples	Content of Element by Atomic (%)					S_{BET} (m^2/g)	Pore volume (cm^2/g)	Average pore diameter (nm)	Total area in pores (m^2/g)	Total volume in pores (cm^3/g)
	Zn	O	Na	K	N					
zNaOH	37.50	41.37	21.13	-	-	14.10	0.099	28.77	8.80	0.047
zKOH	44.96	54.96	-	0.08	-	15.31	0.129	34.17	9.49	0.057
zNH_4OH	42.85	53.81	-	-	3.34	6.11	0.026	14.65	4.85	0.019
z$NaHCO_3$	53.11	34.05	12.84	-	-	5.26	0.015	10.37	3.64	0.010

3.4 Photocatalytic activity

To investigate the photocatalytic efficiency of all prepared ZnO nanoparticles, the degradation of basic blue41 (BB41), acid orange7 (AO7), and methylene blue (MB) after exposure to the UV light source was used to estimate the photocatalytic efficiency of ZnO samples. BB41 and AO7 are two unique azo dyes with distinct chemical structures and properties. The difference in charge between BB41 (positive dye) and AO7 (negative dye) was utilized to investigate charge-selective absorption on the surface of the catalyst. Additionally, the efficiency of the catalyst in the photodegradation of complex dye structures was evaluated using MB, which was classified as a thiazine dye. The absorption spectra in the photodegradation of BB41, AO7, and MB exhibited characteristic absorption bands centered at 609 nm, 485 nm, and 664 nm, respectively. For the removal efficiency of all synthesized ZnO, the z$NaHCO_3$ exhibited the highest efficiency for BB41, AO7, and MB in comparison with other catalysts, as shown in Figure 8. The photocatalytic efficiency of z$NaHCO_3$ was found to be 96.90, 48.92, and 74.12% for degradation of BB41, AO7, and MB, respectively. The photocatalytic efficiency of zNaOH was 60.43, 28.80, and 28.55% for degradation of BB41, AO7, and MB, respectively. The zKOH sample presented a photocatalytic performance of 54.10, 26.82, and 21.73% for degradation of BB41, AO7, and MB, respectively. Moreover, the lowest performance of zNH_4OH as a photocatalyst for photodegradation of BB41, AO7, and MB was observed in the experiment, which exhibited a degradation of 39.48, 7.80, and 12.44%, respectively.

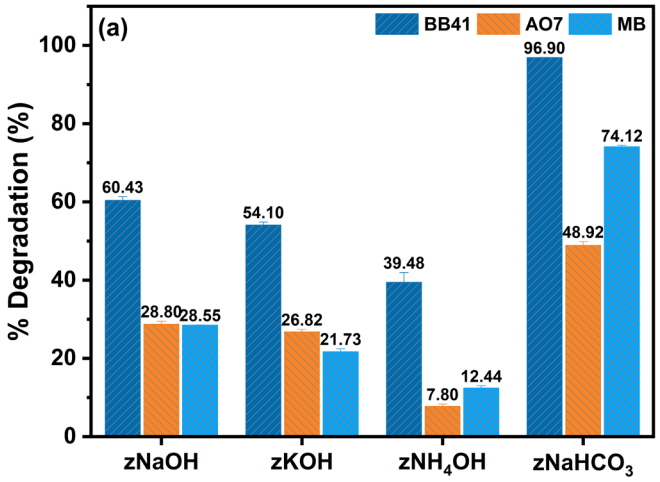

Figure 8. Removal efficiency of ZnO prepared with different types of bases for the degradation of BB41, AO7, and MB under UV irradiation time of 3 h.

In analyzing the factors influencing the dye degradation efficiency of ZnO nanocrystals based on the provided data and experimental results, the relationship between crystallite size, surface area, band gap, and oxygen vacancies significantly affected performance outcomes. Larger crystallite sizes, greater surface areas, higher band gaps, and more oxygen vacancies all correlated positively with dye degradation efficiency (Dodd et al., 2006; Pardeshi & Patil, 2009; Becker et al., 2011; Wang et al., 2012; Flores et al., 2014; Klubnuan et al., 2016; Xie et al., 2020; He et al., 2022; Ranjbari et al., 2024). The experimental findings indicated the following order of dye degradation efficiency: $zNaHCO_3$ > zNaOH > zKOH > zNH_4OH. This observed order contrasted with initial predictions based solely on individual parameter analysis, suggesting a more complex interplay among these factors. ZnO synthesized from $NaHCO_3$ exhibited the highest photodegradation efficiency, despite having the lowest surface area (5.26 m^2/g). This superior performance is attributed to the largest crystallite size (49.10 nm) and the highest band gap (3.13 eV). The large crystallite size provides more active sites for photocatalytic reaction. Generally, the {001} facets of ZnO are polar surfaces or active surfaces, which exhibit the highest catalytic activity (Chen et al., 2015; Yang et al., 2021). These polar surfaces readily absorb O_2 and H_2O molecules, resulting in a higher production rate of reactive species and promoting photocatalytic reaction (Yang et al., 2012). The exposure of {001} facets corresponds to the (002) diffraction peak in the XRD data. The activity of the {001} facet is associated with its higher energy compared to other faces of ZnO. The charge on the facet potentially attracts H_2O, which may accelerate the generation of reactive species ($^{\bullet}OH$ and $O_2^{-\bullet}$), leading to higher efficiency in dye degradation during photocatalysis. Thus, the highest photocatalytic efficiency of $zNaHCO_3$ is due to the largest crystallite size at the (002) crystal plane, which produces the most reactive species for the decomposition of organic contaminants. Additionally, a high band gap enhances the ability of a material to absorb UV light and generate electron-hole pairs, which further reduces the recombination rate and is essential for the degradation process. This is because the increased absorption of UV light leads to more efficient generation of charge carriers that are less likely to recombine due to the higher energy separation (Nazarov et al., 2018).

ZnO synthesized from NaOH also showed high efficiency due to a combination of significant crystallite size (35.54 nm), surface area (14.10 m^2/g), moderately high band gap (2.99 eV), and oxygen vacancies. This combination indicates that a relatively large crystallite size and adequate band gap, along with the presence of oxygen vacancies, facilitates effective dye degradation. A moderate crystallite size supports the reaction by providing enough active sites, while oxygen vacancies enhance photocatalytic activity by creating additional reactive sites and trapping electrons, reducing the recombination of electron-hole pairs. This increases the availability of charge carriers for redox reactions, leading to more reactive oxygen species that effectively degrade organic contaminants (Zhang et al., 2018; Ranjbari et al., 2023).

Additionally, ZnO synthesized from KOH showed moderate efficiency despite having the highest surface area (15.31 m^2/g). The smaller crystallite size (33.42 nm), lower band gap (2.97 eV), and oxygen vacancies contributed to its overall reduced effectiveness. Although a higher number of oxygen vacancies provides additional reactive sites for the photocatalytic reaction, a smaller crystallite size and lower band gap limit the absorption of UV light and the stability of active sites, thus reducing the overall efficiency. Comparing the two, zNaOH benefits from a balanced combination of crystallite size, surface area, and band gap, which collectively enhance its photocatalytic performance. Meanwhile, zKOH, despite having the highest surface area, suffered from smaller crystallite size and lower band gap, which hindered its ability to effectively absorb UV light and maintain stable active sites, resulting in lower overall efficiency. ZnO synthesized from NH_4OH had the lowest efficiency, likely due to its smallest crystallite size (23.83 nm) and lowest surface area (6.11 m^2/g). This combination of unfavorable factors resulted in fewer active sites, leading to reduced photocatalytic activity. The high number of oxygen vacancies in zNH_4OH provided additional reactive sites, however, these were not sufficient to overcome the limitations posed by the other factors.

Comparing the bases used for ZnO synthesis, it is evident that the choice of base significantly influences the material properties and photocatalytic performance. NaOH and $NaHCO_3$ yielded materials with larger crystallite sizes, which were beneficial for photodegradation. $NaHCO_3$ produced ZnO with the highest efficiency due to the optimal combination of large crystallite size and high band gap. KOH, while producing ZnO with the highest surface area, did not achieve the highest efficiency due to other limiting factors such as smaller crystallite size and lower band gap. NH_4OH produced ZnO with the lowest efficiency, indicating that it may not be the most suitable base for synthesizing highly efficient ZnO photocatalysts. These findings suggest that while surface area is important, the combined effects of larger crystallite size, optimal band gap, and more oxygen vacancies are more critical in determining the photocatalytic efficiency of ZnO in dye degradation. The study highlights the complexity of material properties and their synergistic effects on photocatalytic performance. It demonstrates that optimizing multiple factors rather than focusing on a single property is essential for enhancing the efficiency of ZnO photocatalysts. ZnO synthesized from $NaHCO_3$, despite its lower surface area, demonstrated the highest dye degradation efficiency due to its favorable crystallite size, band gap, and oxygen vacancy characteristics. This insight could guide the development of more effective photocatalysts for environmental remediation and other applications.

To study the mechanism of the photodegradation of organic dyes using the ZnO nanoparticles, an experiment using scavengers was conducted to elucidate the role of specific reactive oxygen species (ROS) in the photocatalytic process. In photocatalysis, various ROS such as h^+, $^{\bullet}OH$, e^-, and $O_2^{-\bullet}$ can be generated and can interact with the dyes. The addition of the scavengers, including 10 mM sodium oxalate (h^+ scavenger), 10 mM isopropanol ($^{\bullet}OH$ scavenger), and 10 mM p-benzoquinone ($O_2^{-\bullet}$ scavenger) significantly

reduced the photocatalytic efficiency of $zNaHCO_3$. As illustrated in Figure 9, the photocatalytic efficiencies were 96.90%, 85.21%, 53.05%, and 6.57% for the samples without a scavenger, and with sodium oxalate (SO), p-benzoquinone (PBQ), and isopropanol (IPA), respectively. These results indicate that the presence of p-benzoquinone and isopropanol as scavengers greatly affected and decreased the photocatalytic efficiency relative to the control. Additionally, a minor decrease was observed when sodium oxalate was employed as a scavenger. Therefore, it can be inferred that superoxide ($O_2^{-\bullet}$) and hydroxyl ($^{\bullet}OH$) radicals were the predominant ROS species influencing the photocatalytic efficiency of $zNaHCO_3$. In summary, the order of dominance of ROS species in the photocatalytic process can be estimated as $^{\bullet}OH > O_2^{-\bullet} > h^+$.

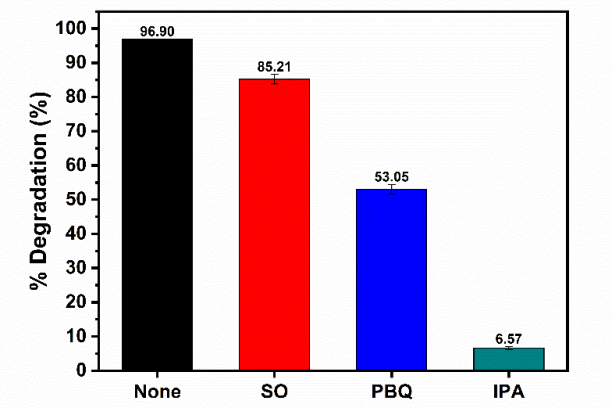

Figure 9. The effect of scavengers on the photodegradation of 10 ppm BB41 by $zNaHCO_3$ (20 mg/L) under UV irradiation for 3 h.

The findings of this research underscored the critical role of base precursors in shaping the environmental performance of ZnO nanoparticles. The preference for $NaHCO_3$ as a base precursor highlighted the importance of considering environmental aspects in nanoparticle synthesis procedures. The improved photocatalytic efficiency of ZnO nanoparticles synthesized with $NaHCO_3$ had significant implications for environmental remediation efforts. These photocatalysts offer a sustainable method for combating water pollution and preserving aquatic ecosystems by efficiently degrading dye pollutants found in wastewater. Additionally, using $NaHCO_3$ as a benign and environmentally friendly base precursor is in alignment with the principles of green chemistry, which aims to minimize the production of hazardous by-products and decrease the overall environmental impact of the synthesis process.

4. Conclusions

ZnO nanoparticles were synthesized via a simple precipitation method using different basic solutions, including NaOH, KOH, NH_4OH, or $NaHCO_3$. The basicity of the resulting solution was varied by employing different types of basic solutions, which significantly influenced the formation of intermediate compounds and ions. Each base has a distinct dissociation constant (K_b) that influences the hydroxide precursor, thereby directly affecting the formation of intermediates and ZnO nanoparticles. The results indicated that intermediate formation played an important role in the growth mechanism of ZnO nanoparticles,

affecting their morphology, crystallite size, crystallinity, and lattice strain. The presence of ions from various basic solutions in the ZnO structure caused variations in the color and the band gap energy of the ZnO samples. The photodegradation efficiency of the synthesized ZnO nanoparticles was evaluated using various organic dyes (BB41, AO7, and MB) under UV light irradiation. Among the photocatalysts, z$NaHCO_3$ exhibited the highest dye removal efficiency, attributed to its high crystallinity and large crystallite size. The addition of scavengers indicated that hydroxyl ($^{\bullet}OH$) was the predominant reactive oxygen species that influenced the photocatalytic efficiency of z$NaHCO_3$.

5. Acknowledgements

This research was supported by Science Achievement Scholarship of Thailand (SAST). The authors would like to thank laboratory 502, Department of Chemistry, Faculty of Science, Kasetsart University for the facilities.

6. Conflicts of Interest

The authors declare no conflict of interest.

References

Abdulrahman, A. F., Ahmed, S. M., Hamad, S. M., Almessiere, M. A., Ahmed, N. M., & Sajadi, S. M. (2021). Effect of different pH values on growth solutions for the ZnO nanostructures. *Chinese Journal of Physics*, 71, 175-189. https://doi.org/10.1016/j.cjph.2021.02.013

Agarwal, S., Jangir, L. K., Rathore, K. S., Kumar, M., & Awasthi, K. (2019). Morphology-dependent structural and optical properties of ZnO nanostructures. *Applied Physics. A*, 125(8), Article 553. https://doi.org/10.1007/s00339-019-2852-x

Ahmad, I., Aslam, M., Jabeen, U., Zafar, M. N., Malghani, M. N. K., Alwadai, N., Alshammari, F. H., Almuslem, A. S., & Ullah, Z. (2022). ZnO and Ni-doped ZnO photocatalysts: Synthesis, characterization and improved visible light driven photocatalytic degradation of methylene blue. *Inorganica Chimica Acta*, 543, Article 121167. https://doi.org/10.1016/j.ica.2022.121167

Al-Tohamy, R., Ali, S. S., Li, F., Okasha, K. M., Mahmoud, Y. A.-G., Elsamahy, T., Jiao, H., Fu, Y., & Sun, J. (2022). A critical review on the treatment of dye-containing wastewater: Ecotoxicological and health concerns of textile dyes and possible remediation approaches for environmental safety. *Ecotoxicology and Environmental Safety*, 231, Article 113160. https://doi.org/10.1016/j.ecoenv.2021.113160

Al-Gaashani, R., Radiman, S., Daud, A. R., Tabet, N., & Al-Douri, Y. (2013). XPS and optical studies of different morphologies of ZnO nanostructures prepared by microwave methods. *Ceramics International*, 39(3), 2283-2292. https://doi.org/10.1016/j.ceramint.2012.08.075

Alanazi, H. S., Ahmad, N., & Alharthi, F. A. (2021). Synthesis of Gd/N co-doped ZnO for enhanced UV-vis and direct solar-light-driven photocatalytic degradation. *RSC Advances*, 11(17), 10194-10202. https://doi.org/10.1039/d0ra10698d

Aracena, A., Pino, J., & Jerez, O. (2020). Mechanism and kinetics of malachite dissolution in an NH_4OH system. *Metals*, 10(6), Article 833. https://doi.org/10.3390/met10060833

Arellano-Cortaza, M., Ramírez-Morales, E., Pal, U., Pérez-Hernández, G., & Rojas-Blanco, L. (2021). pH dependent morphology and texture evolution of ZnO nanoparticles

fabricated by microwave-assisted chemical synthesis and their photocatalytic dye degradation activities. *Ceramics International*, 47(19), 27469-27478. https://doi.org/10.1016/j.ceramint.2021.06.170

Ashraf, R., Riaz, S., Hussain, S. S., & Naseem, S. (2015). Effect of pH on properties of ZnO nanoparticles. *Materials Today: Proceedings*, 2(10), 5754-5759. https://doi.org/10.1016/j.matpr.2015.11.123

Auer, M., Wölfler, C., & Antrekowitsch, J. (2022). Influence of different carbon content on reduction of zinc oxide via metal bath. *Applied Sciences*, 12(2), Article 664. https://doi.org/10.3390/app12020664

Ayoub, I., Kumar, V., Abolhassani, R., Sehgal, R., Sharma, V., Sehgal, R., Swart, H. C., & Mishra, Y. K. (2022). Advances in ZnO: Manipulation of defects for enhancing their technological potentials. *Nanotechnology Reviews*, 11(1), 575-619. https://doi.org/10.1515/ntrev-2022-0035

Bao, H. V., Dat, N. M., Giang, N. T. H., Thinh, D. B., Tai, L. T., Trinh, D. N., Hai, N. D., Khoa, N. A. D., Huong, L. M., Nam, H. M., Phong, M. T., & Hieu, N. H. (2021). Behavior of ZnO-doped TiO_2/rGO nanocomposite for water treatment enhancement. *Surfaces and Interfaces*, 23, Article 100950. https://doi.org/10.1016/j.surfin.2021.100950

Baruah, S., & Dutta, J. (2009). Hydrothermal growth of ZnO nanostructures. *Science and Technology of Advanced Materials*, 10(1), Article 013001. https://doi.org/10.1088/1468-6996/10/1/013001

Bashir, M., Majid, F., Bibi, I., Mushtaq, J., Ali, A., Farhat, L. B., Katubi, K. M., Alwadai, N., Khan, M. I., & Iqbal, M. (2022). Ultrasonic assisted synthesis of ZnO nanoflakes and photocatalytic activity evaluation for the degradation of methyl orange. *Arabian Journal of Chemistry*, 15(11), Article 104194. https://doi.org/10.1016/j.arabjc.2022.104194

Becker, J., Raghupathi, K. R., St. Pierre, J., Zhao, D., & Koodali, R. T. (2011). Tuning of the crystallite and particle sizes of ZnO nanocrystalline materials in solvothermal synthesis and their photocatalytic activity for dye degradation. *The Journal of Physical Chemistry C*, 115(28), 13844-13850. https://doi.org/10.1021/jp2038653

Benhebal, H., Chaib, M., Malengreaux, C., Lambert, S. D., Leonard, A., Crine, M., & Heinrichs, B. (2014). Visible-light photo-activity of alkali metal doped ZnO. *Journal of the Taiwan Institute of Chemical Engineers*, 45(1), 249-253. https://doi.org/10.1016/j.jtice.2013.04.003

Bhattacharyya, S., & Gedanken, A. (2008). A template-free, sonochemical route to porous ZnO nano-disks. *Microporous and Mesoporous Materials*, 110(2-3), 553-559. https://doi.org/10.1016/j.micromeso.2007.06.053

Chandrappa, K. G., & Venkatesha, T. V. (2012). Electrochemical synthesis and photocatalytic property of Zinc oxide nanoparticles. *Nano-Micro Letters*, 4(1), 14-24. https://doi.org/10.1007/bf03353686

Chen, L.-L., Zhai, B.-G., & Huang, Y. M. (2020). Rendering visible-light photocatalytic activity to undoped ZnO via intrinsic defects engineering. *Catalysts*, 10(10), Article 1163. https://doi.org/10.3390/catal10101163

Chen, Y., Zhao, H., Liu, B., & Yang, H. (2015). Charge separation between wurtzite ZnO polar {0 0 1} surfaces and their enhanced photocatalytic activity. *Applied Catalysis B: Environmental*, 163, 189-197. https://doi.org/10.1016/j.apcatb.2014.07.044

Chithra, M. J., Sathya, M., & Pushpanathan, K. (2015). Effect of pH on crystal size and photoluminescence property of ZnO nanoparticles prepared by chemical precipitation method. *Acta Metallurgica Sinica (English Letters)*, 28(3), 394-404. https://doi.org/10.1007/s40195-015-0218-8

Claros, M., Setka, M., Jimenez, Y. P., & Vallejos, S. (2020). AACVD synthesis and characterization of iron and copper oxides modified ZnO structured films. *Nanomaterials*, 10(3), Article 471. https://doi.org/10.3390/nano10030471

Das, S. C., Green, R. J., Podder, J., Regier, T. Z., Chang, G. S., & Moewes, A. (2013). Band gap tuning in ZnO through Ni doping via spray pyrolysis. *The Journal of Physical Chemistry C,* 117(24), 12745-12753. https://doi.org/10.1021/jp3126329

Dey, S., Das, S., & Kar, A. K. (2021). Role of precursor dependent nanostructures of ZnO on its optical and photocatalytic activity and influence of FRET between ZnO and methylene blue dye on photocatalysis. *Materials Chemistry and Physics*, 270, Article 124872. https://doi.org/10.1016/j.matchemphys.2021.124872

Dhir, R. (2020). Photocatalytic degradation of methyl orange dye under UV irradiation in the presence of synthesized PVP capped pure and gadolinium doped ZnO nanoparticles. *Chemical Physics Letters*, 746, Article 137302. https://doi.org/10.1016/j.cplett.2020.137302

Dodd, A. C., McKinley, A. J., Saunders, M., & Tsuzuki, T. (2006). Effect of particle size on the photocatalytic activity of nanoparticulate zinc oxide. *Journal of Nanoparticle Research*, 8(1), 43-51. https://doi.org/10.1007/s11051-005-5131-z

Droepenu, E., Wee, B., Chin, S., Kok, K., & Asare, E. (2020). Synthesis and Characterization of Single Phase ZnO Nanostructures via Solvothermal Method: Influence of Alkaline Source. *Biointerface Research in Applied Chemistry*, 10, 5648-5655. https://doi.org/10.33263/briac103.648655

Eikeland, A. Z., Hölscher, J., & Christensen, M. (2021). Hydrothermal synthesis of SrFe12O19 nanoparticles: effect of the choice of base and base concentration. *Journal of Physics D: Applied Physics*, 54(13), Article 134004. https://doi.org/10.1088/1361-6463/abd2ec

Erdogan, N. H., Kutlu, T., Sedefoglu, N., & Kavak, H. (2021). Effect of Na doping on microstructures, optical and electrical properties of ZnO thin films grown by sol-gel method. *Journal of Alloys and Compounds*, 881, Article 160554. https://doi.org/10.1016/j.jallcom.2021.160554

Ferreira, S. H., Morais, M., Nunes, D., Oliveira, M. J., Rovisco, A., Pimentel, A., Águas, H., Fortunato, E., & Martins, R. (2021). High UV and sunlight photocatalytic performance of porous ZnO nanostructures synthesized by a facile and fast microwave hydrothermal method. *Materials*, 14(9). Article 2385. https://doi.org/10.3390/ma14092385

Flores, N. M., Pal, U., Galeazzi, R., & Sandoval, A. (2014). Effects of morphology, surface area, and defect content on the photocatalytic dye degradation performance of ZnO nanostructures. *RSC Advances*, 4(77), 41099-41110. https://doi.org/10.1039/c4ra04522j

Galmiz, O., Stupavska, M., Wulff, H., Kersten, H., Brablec, A., & Cernak, M. (2015). Deposition of Zn-containing films using atmospheric pressure plasma jet. *Open Chemistry*, 13(1), 198-203. https://doi.org/10.1515/chem-2015-0020

Gnanaprakasam, A., Sivakumar, V. M., & Thirumarimurugan, M. (2015). Influencing parameters in the photocatalytic degradation of organic effluent via nanometal oxide catalyst: A review. *Indian Journal of Materials Science*, 2015, 1-16. https://doi.org/10.1155/2015/601827

He, L., Tong, Z., Wang, Z., Chen, M., Huang, N., & Zhang, W. (2018). Effects of calcination temperature and heating rate on the photocatalytic properties of ZnO prepared by pyrolysis. *Journal of Colloid and Interface Science*, 509, 448-456. https://doi.org/10.1016/j.jcis.2017.09.021

He, X., Yang, Y., Li, Y., Chen, J., Yang, S., Liu, R., & Xu, Z. (2022). Effects of structure and surface properties on the performance of ZnO towards photocatalytic degradation of methylene blue. *Applied Surface Science*, 599, Article 153898. https://doi.org/10.1016/j.apsusc.2022.153898

Hu, X.-L., Zhu, Y.-J., & Wang, S.W. (2004). Sonochemical and microwave-assisted synthesis of linked single-crystalline ZnO rods. *Materials Chemistry and Physics*, 88(2-3), 421-426. https://doi.org/10.1016/j.matchemphys.2004.08.010

Ismail, A. A., El-Midany, A., Abdel-Aal, E. A., & El-Shall, H. (2005). Application of statistical design to optimize the preparation of ZnO nanoparticles via hydrothermal technique. *Materials Letters*, 59(14-15), 1924-1928. https://doi.org/10.1016/j.matlet.2005.02.027

Jiang, Y., Sun, Y., Liu, H., Zhu, F., & Yin, H. (2008). Solar photocatalytic decolorization of C.I. Basic Blue 41 in an aqueous suspension of TiO_2–ZnO. *Dyes and Pigments: An International Journal*, 78(1), 77-83. https://doi.org/10.1016/j.dyepig.2007.10.009

Karpińska, J., & Kotowska, U. (2019). Removal of organic pollution in the water environment. *Water*, 11(10), Article 2017. https://doi.org/10.3390/w11102017

Klubnuan, S., Suwanboon, S., & Amornpitoksuk, P. (2016). Effects of optical band gap energy, band tail energy and particle shape on photocatalytic activities of different ZnO nanostructures prepared by a hydrothermal method. *Optical Materials*, 53, 134-141. https://doi.org/10.1016/j.optmat.2016.01.045

Kołodziejczak-Radzimska, A., & Jesionowski, T. (2014). Zinc oxide-from synthesis to application: A review. *Materials*, 7(4), 2833-2881. https://doi.org/10.3390/ma7042833

Kołodziejczak-Radzimska, A., Markiewicz, E., & Jesionowski, T. (2012). Structural characterisation of ZnO particles obtained by the emulsion precipitation method. *Journal of Nanomaterials*, 2012, 1-9. https://doi.org/10.1155/2012/656353

Kumar, A., & Ahmad, I. (2020). Role of defects and microstructure on the electrical properties of solution-processed Al-doped ZnO transparent conducting films. *Applied Physics. A. Materials Science & Processing*, 126(8), Article 598. https://doi.org/10.1007/s00339-020-03767-0

Kumar, K. M., Mandal, B. K., Naidu, E. A., Sinha, M., Kumar, K. S., & Reddy, P. S. (2013). Synthesis and characterisation of flower shaped zinc oxide nanostructures and its antimicrobial activity. *Spectrochimica Acta Part A: Molecular and Biomolecular Spectroscopy*, 104, 171-174. https://doi.org/10.1016/j.saa.2012.11.025

Kumari, R., Sahai, A., & Goswami, N. (2015). Effect of nitrogen doping on structural and optical properties of ZnO nanoparticles. *Progress in Natural Science: Materials International*, 25(4), 300-309. https://doi.org/10.1016/j.pnsc.2015.08.003

Kwoka, M., Kulis-Kapuscinska, A., Zappa, D., Comini, E., & Szuber, J. (2020). Novel insight on the local surface properties of ZnO nanowires. *Nanotechnology*, 31(46), Article 465705. https://doi.org/10.1088/1361-6528/ab8dec

Lamba, Randeep, Umar, A., Mehta, S. K., & Kansal, S. K. (2015). CeO_2ZnO hexagonal nanodisks: Efficient material for the degradation of direct blue 15 dye and its simulated dye bath effluent under solar light. *Journal of Alloys and Compounds*, 620, 67-73. https://doi.org/10.1016/j.jallcom.2014.09.101

Lamba, R., Umar, A., Mehta, S., & Kansal, S. K. (2017). Enhanced visible light driven photocatalytic application of Ag_2O decorated ZnO nanorods heterostructures. *Separation and Purification Technology*, 183, 341-349

Lee, Y. C., Yang, C. S., Huang, H. J., Hu, S. Y., Lee, J. W., Cheng, C. F., Huang, C. C., Tsai, M. K., & Kuang, H. C. (2010). Structural and optical properties of ZnO nanopowder prepared by microwave-assisted synthesis. *Journal of Luminescence*, 130(10), 1756-1759. https://doi.org/10.1016/j.jlumin.2010.04.005

Lew, S., Sarofim, A. F., & Flytzani-Stephanopoulos, M. (1992). The reduction of zinc titanate and zinc oxide solids. *Chemical Engineering Science*, 47(6), 1421-1431. https://doi.org/10.1016/0009-2509(92)80287-m

Limón-Rocha, I., Guzmán-González, C. A., Anaya-Esparza, L. M., Romero-Toledo, R., Rico, J. L., González-Vargas, O. A., & Pérez-Larios, A. (2022). Effect of the precursor

on the synthesis of ZnO and its photocatalytic activity. *Inorganics*, 10(2), Article 16. https://doi.org/10.3390/inorganics10020016

Lin, Z., Guo, F., Wang, C., Wang, X., Wang, K., & Qu, Y. (2014). Preparation and sensing properties of hierarchical 3D assembled porous ZnO from zinc hydroxide carbonate. *RSC Advances*, 4(10), Article 5122. https://doi.org/10.1039/c3ra45254a

Liu, N., Pidaparti, R., & Wang, X. (2018). Abnormal linear elasticity in polycrystalline phosphorene. *Physical Chemistry Chemical Physics*, 20(13), 8668–8675. https://doi.org/10.1039/c7cp08540k

Lucentini, I., Garcia, X., Vendrell, X., & Llorca, J. (2021). Review of the decomposition of ammonia to generate hydrogen. *Industrial and Engineering Chemistry Research*, 60(51), 18560-18611. https://doi.org/10.1021/acs.iecr.1c00843

Manzoor, U., Islam, M., Tabassam, L., & Rahman, S. U. (2009). Quantum confinement effect in ZnO nanoparticles synthesized by co-precipitate method. *Physica E: Low-Dimensional Systems & Nanostructures*, 41(9), 1669-1672. https://doi.org/10.1016/j.physe.2009.05.016

Marinho, J. Z., de Paula, L. F., Longo, E., Patrocinio, A. O. T., & Lima, R. C. (2019). Effect of Gd^{3+} doping on structural and photocatalytic properties of ZnO obtained by facile microwave-hydrothermal method. *SN Applied Sciences*, 1(4), Article 359. https://doi.org/10.1007/s42452-019-0359-x

McCluskey, M. D., & Jokela, S. J. (2009). Defects in ZnO. *Journal of Applied Physics*, 106(7). Article 071101. https://doi.org/10.1063/1.3216464

McLaren, A., Valdes-Solis, T., Li, G., & Tsang, S. C. (2009). Shape and size effects of ZnO nanocrystals on photocatalytic activity. *Journal of the American Chemical Society*, 131(35), 12540-12541. https://doi.org/10.1021/ja9052703

Modwi, A., Khezami, L., Taha, K. K., Bessadok J., A., & Mokraoui, S. (2019). Photo-degradation of a mixture of dyes using Barium doped ZnO nanoparticles. *Journal of Materials Science: Materials in Electronics*, 30(15), 14714-14725. https://doi.org/10.1007/s10854-019-01843-7

Moghri Moazzen, M. A., Borghei, S. M., & Taleshi, F. (2013). Change in the morphology of ZnO nanoparticles upon changing the reactant concentration. *Applied Nanoscience*, 3(4), 295-302. https://doi.org/10.1007/s13204-012-0147-z

Moussa, N. B., Lajnef, M., Jebari, N., Villebasse, C., Bayle, F., Chaste, J., Madouri, A., Chtourou, R., & Herth, E. (2021). Synthesis of ZnO sol-gel thin-films CMOS-Compatible. *RSC Advances*, 11(37), 22723-22733. https://doi.org/10.1039/d1ra02241e

Nageeb, M. (2013). Adsorption technique for the removal of organic pollutants from water and wastewater. *Organic pollutants - monitoring, risk and treatment*. InTech.

Nazarov, A. E., Eloev, G. G., & Ivanov, A. I. (2018). Effect of charge separation free energy gap on the rate constant of ultrafast charge recombination in ion pairs formed by intramolecular photoinduced electron transfer. *Journal of Photochemistry and Photobiology A: Chemistry*, 358, 207-214. https://doi.org/10.1016/j.jphotochem.2018.03.017

Nezamzadeh-Ejhieh, A., & Khorsandi, S. (2014). Photocatalytic degradation of 4-nitrophenol with ZnO supported nano-clinoptilolite zeolite. *Journal of Industrial and Engineering Chemistry*, 20(3), 937-946. https://doi.org/10.1016/j.jiec.2013.06.026

Nguyen, T. L., & Saleh, M. A. (2020). Thermal degradation of azobenzene dyes. *Results in Chemistry*, 2, Article 100085. https://doi.org/10.1016/j.rechem.2020.100085

Ong, C. B., Ng, L. Y., & Mohammad, A. W. (2018). A review of ZnO nanoparticles as solar photocatalysts: Synthesis, mechanisms and applications. *Renewable and Sustainable Energy Reviews*, 81, 536-551. https://doi.org/10.1016/j.rser.2017.08.020

Pandey, Monica, Singh, M., Wasnik, K., Gupta, S., Patra, S., Gupta, P. S., Pareek, D., Chaitanya, N. S. N., Maity, S., Reddy, A. B. M., Tilak, R., & Paik, P. (2021). Targeted

and enhanced antimicrobial inhibition of mesoporous ZnO-Ag_2O/Ag, ZnO-CuO, and ZnO-SnO_2 composite nanoparticles. *ACS Omega*, 6(47), 31615-31631. https://doi.org/10.1021/acsomega.1c04139

Pardeshi, S. K., & Patil, A. B. (2009). Effect of morphology and crystallite size on solar photocatalytic activity of zinc oxide synthesized by solution free mechanochemical method. *Journal of Molecular Catalysis A: Chemical*, 308(1-2), 32-40. https://doi.org/10.1016/j.molcata.2009.03.023

Park, S. Y., Kim, S., Yoo, J., Lim, K.-H., Lee, E., Kim, K., Kim, J., & Kim, Y. S. (2014). Aqueous zinc ammine complex for solution-processed ZnO semiconductors in thin film transistors. *RSC Advances*, 4(22), Article 11295. https://doi.org/10.1039/c3ra47437b

Qi, J., & Hu, X. (2020). The loss of ZnO as the support for metal catalysts by H_2 reduction. *Physical Chemistry Chemical Physics*, 22(7), 3953-3958. https://doi.org/10.1039/c9cp06093f

Rabin, N. N., Morshed, J., Akhter, H., Islam, M. S., Hossain, M. A., Elias, M., Alam, M. M., Karim, M. R., Hasnat, M. A., Uddin, M. N., & Siddiquey, I. A. (2016). Surface modification of the ZnO nanoparticles with γ-aminopropyltriethoxysilane and study of their photocatalytic activity, optical properties and antibacterial activities. *International Journal of Chemical Reactor Engineering*, 14(3), 785-794. https://doi.org/10.1515/ijcre-2015-0141

Rahman, M. R., Uddin, M. N., Ashrafy, T., Washif, M., Uddin, M. R., Hoq, M., & Jalal, A. H. (2022). Tuning of optical band gap: Genesis of thickness regulated Al doped ZnO nano-crystalline thin films formulated by sol–gel spin coating approach. *Transactions on Electrical and Electronic Materials*, 23(3), 205-218. https://doi.org/10.1007/s42341-021-00341-0

Raj, K. P., & Sadayandi, K. (2016). Effect of temperature on structural, optical and photoluminescence studies on ZnO nanoparticles synthesized by the standard co-precipitation method. *Physica B: Condensed Matter*, 487, 1-7. https://doi.org/10.1016/j.physb.2016.01.020

Rajamanickam, D., & Shanthi, M. (2016). Photocatalytic degradation of an organic pollutant by zinc oxide – solar process. *Arabian Journal of Chemistry*, 9, S1858-S1868. https://doi.org/10.1016/j.arabjc.2012.05.006

Ranjbari, A., Demeestere, K., Kim, K.-H., & Heynderickx, P. M. (2023). Oxygen vacancy modification of commercial ZnO by hydrogen reduction for the removal of thiabendazole: Characterization and kinetic study. *Applied Catalysis B: Environmental*, 324, Article 122265. https://doi.org/10.1016/j.apcatb.2022.122265

Ranjbari, A., Kim, J., Yu, J., Kim, J., Park, M., Kim, N., Demeestere, K., & Heynderickx, P. M. (2024). Effect of oxygen vacancy modification of ZnO on photocatalytic degradation of methyl orange: A kinetic study. *Catalysis Today*, 427, Article 114413. https://doi.org/10.1016/j.cattod.2023.114413

Razavi-Khosroshahi, H., Edalati, K., Wu, J., Nakashima, Y., Arita, M., Ikoma, Y., Sadakiyo, M., Inagaki, Y., Staykov, A., Yamauchi, M., Horita, Z., & Fuji, M. (2017). High-pressure zinc oxide phase as visible-light-active photocatalyst with narrow band gap. *Journal of Materials Chemistry. A, Materials for Energy and Sustainability*, 5(38), 20298-20303. https://doi.org/10.1039/c7ta05262f

Reli, M., Edelmannová, M., Šihor, M., Praus, P., Svoboda, L., Mamulová, K. K., Otoupalíková, H., Čapek, L., Hospodková, A., Obalová, L., & Kočí, K. (2015). Photocatalytic H_2 generation from aqueous ammonia solution using ZnO photocatalysts prepared by different methods. *International Journal of Hydrogen Energy*, 40(27), 8530-8538. https://doi.org/10.1016/j.ijhydene.2015.05.004

Remor, P. V., Bastos, J. A., Alino, J. H. L., Frare, L. M., Kaparaju, P., & Edwiges, T. (2023). Optimization of chemical solution concentration and exposure time in the alkaline pretreatment applied to sugarcane bagasse for methane production. *Environmental Technology*, 44(19), 2843-2855. https://doi.org/10.1080/09593330.2022.2046645

Sahai, A., & Goswami, N. (2014). Probing the dominance of interstitial oxygen defects in ZnO nanoparticles through structural and optical characterizations. *Ceramics International*, 40(9), 14569-14578. https://doi.org/10.1016/j.ceramint.2014.06.041

Sahu, J., Kumar, S., Vats, V. S., Alvi, P. A., Dalela, B., Phase, D. M., Gupta, M., Kumar, S., & Dalela, S. (2022). Role of defects and oxygen vacancy on structural, optical and electronic structure properties in Sm-substituted ZnO nanomaterials. *Journal of Materials Science: Materials in Electronics*, 33(27), 21546-21568. https://doi.org/10.1007/s10854-022-08945-9

Sansenya, T., Masri, N., Chankhanittha, T., Senasu, T., Piriyanon, J., Mukdasai, S., & Nanan, S. (2022). Hydrothermal synthesis of ZnO photocatalyst for detoxification of anionic azo dyes and antibiotic. *The Journal of Physics and Chemistry of Solids*, 160, Article 110353. https://doi.org/10.1016/j.jpcs.2021.110353

Sasaoka, E., Hirano, S., Kasaoka, S., & Sakata, Y. (1994). Stability of zinc oxide high-temperature desulfurization sorbents for reduction. *Energy and Fuels*, 8(3), 763-769. https://doi.org/10.1021/ef00045a033

Selvaraj, S., Mohan, M. K., Navaneethan, M., Ponnusamy, S., & Muthamizhchelvan, C. (2019). Synthesis and photocatalytic activity of Gd doped ZnO nanoparticles for enhanced degradation of methylene blue under visible light. *Materials Science in Semiconductor Processing*, 103, Article 104622. https://doi.org/10.1016/j.mssp.2019.104622

Shamsipur, M., Pourmortazavi, S. M., Hajimirsadeghi, S. S., Zahedi, M. M., & Rahimi-Nasrabadi, M. (2013). Facile synthesis of zinc carbonate and zinc oxide nanoparticles via direct carbonation and thermal decomposition. *Ceramics International*, 39(1), 819-827. https://doi.org/10.1016/j.ceramint.2012.07.003

Sharma, D. K., Shukla, S., Sharma, K. K., & Kumar, V. (2022). A review on ZnO: Fundamental properties and applications. *Materials Today: Proceedings*, 49, 3028-3035. https://doi.org/10.1016/j.matpr.2020.10.238

Shen, G.-C., Fujita, S.-I., Matsumoto, S., & Takezawa, N. (1997). Steam reforming of methanol on binary CuZnO catalysts: Effects of preparation condition upon precursors, surface structure and catalytic activity. *Journal of Molecular Catalysis. A, Chemical*, 124(2-3), 123-136. https://doi.org/10.1016/s1381-1169(97)00078-2

Shi, J., Zhang, J., Yang, L., Qu, M., Qi, D.-C., & Zhang, K. H. L. (2021). Wide bandgap oxide semiconductors: From materials physics to optoelectronic devices. *Advanced Materials*, 33(50), Article e2006230. https://doi.org/10.1002/adma.202006230

Singh, M., Goyal, M., & Devlal, K. (2018). Size and shape effects on the band gap of semiconductor compound nanomaterials. *Journal of Taibah University for Science*, 12(4), 470-475. https://doi.org/10.1080/16583655.2018.1473946

Sudha, M., & Rajarajan, M. (2013). Deactivation of photocatalytically active ZnO nanoparticle by surface capping with poly vinyl pyrrolidone. *IOSR Journal of Applied Chemistry*, 3(3), 45-53. https://doi.org/10.9790/5736-0334553

Sulciute, A., Nishimura, K., Gilshtein, E., Cesano, F., Viscardi, G., Nasibulin, A. G., Ohno, Y., & Rackauskas, S. (2021). ZnO nanostructures application in electrochemistry: Influence of morphology. *The Journal of Physical Chemistry. C, Nanomaterials and Interfaces*, 125(2), 1472-1482. https://doi.org/10.1021/acs.jpcc.0c08459

Sun, B., Yang, X., Zhao, D., & Zhang, L. (2018). First-principles study of adsorption mechanism of NH_3 on different ZnO surfaces on organics photocatalytic degradation

purpose. *Computational Materials Science*, 141, 133-140. https://doi.org/10.1016/j.commatsci.2017.09.013

Thongam, D. D., Gupta, J., & Sahu, N. K. (2019). Effect of induced defects on the properties of ZnO nanocrystals: surfactant role and spectroscopic analysis. *SN Applied Sciences*, 1(9), Article 1030. https://doi.org/10.1007/s42452-019-1058-3

Tian, B., Li, C., Gu, F., Jiang, H., Hu, Y., & Zhang, J. (2009). Flame sprayed V-doped TiO_2 nanoparticles with enhanced photocatalytic activity under visible light irradiation. *Chemical Engineering Journal*, 151(1-3), 220-227. https://doi.org/10.1016/j.cej.2009.02.030

Tijani, J. O., Fatoba, O. O., Madzivire, G., & Petrik, L. F. (2014). A review of combined advanced oxidation technologies for the removal of organic pollutants from water. *Water, Air, and Soil Pollution*, 225(9), Article 2102. https://doi.org/10.1007/s11270-014-2102-y

Tinio, J. V. G., Simfroso, K. T., Peguit, A. D. M. V., & Candidato, R. T. (2015). Influence of OH^-ion concentration on the surface morphology of ZnO-SiO_2 nanostructure. *Journal of Nanotechnology*, 2015, 1-7. https://doi.org/10.1155/2015/686021

Uribe-López, M. C., Hidalgo-López, M. C., López-González, R., Frías-Márquez, D. M., Núñez-Nogueira, G., Hernández-Castillo, D., & Alvarez-Lemus, M. A. (2021). Photocatalytic activity of ZnO nanoparticles and the role of the synthesis method on their physical and chemical properties. *Journal of Photochemistry and Photobiology A: Chemistry*, 404, Article 112866. https://doi.org/10.1016/j.jphotochem.2020.112866

Wahab, R., Ansari, S. G., Kim, Y. S., Seo, H. K., Kim, G. S., Khang, G., & Shin, H.S. (2007). Low temperature solution synthesis and characterization of ZnO nano-flowers. *Materials Research Bulletin*, 42(9), 1640-1648. https://doi.org/10.1016/j.materresbull.2006.11.035

Wahab, R., Ansari, S. G., Kim, Y. S., Song, M., & Shin, H.-S. (2009). The role of pH variation on the growth of zinc oxide nanostructures. *Applied Surface Science*, 255(9), 4891-4896. https://doi.org/10.1016/j.apsusc.2008.12.037

Wang, J., Wang, Z., Huang, B., Ma, Y., Liu, Y., Qin, X., Zhang, X., & Dai, Y. (2012). Oxygen vacancy induced band-gap narrowing and enhanced visible light photocatalytic activity of ZnO. *ACS Applied Materials & Interfaces*, 4(8), 4024-4030. https://doi.org/10.1021/am300835p

Wang, V., Ma, D., Jia, W., & Ji, W. (2012). Structural and electronic properties of hexagonal ZnO: A hybrid functional study. *Solid State Communications*, 152(22), 2045-2048. https://doi.org/10.1016/j.ssc.2012.08.024

Weldegebrieal, G. K. (2020). Synthesis method, antibacterial and photocatalytic activity of ZnO nanoparticles for azo dyes in wastewater treatment: A review. *Inorganic Chemistry Communications*, 120, Article 108140. https://doi.org/10.1016/j.inoche.2020.108140

Wittawat, R., Rittipun, R., Jarasfah, M., & Nattaporn, B. (2020). Synthesis of ZnO/TiO2 spherical particles for blue light screening by ultrasonic spray pyrolysis. *Materials Today. Communications*, 24, Article 101126. https://doi.org/10.1016/j.mtcomm.2020.101126

Wu, Y. L., Tok, A. I. Y., Boey, F. Y. C., Zeng, X. T., & Zhang, X. H. (2007). Surface modification of ZnO nanocrystals. *Applied Surface Science*, 253(12), 5473-5479. https://doi.org/10.1016/j.apsusc.2006.12.091

Xie, H., Li, N., Chen, X., Jiang, J., & Zhao, X. (2020). Surface oxygen vacancies promoted photodegradation of benzene on TiO_2 film. *Applied Surface Science*, 511, Article 145597. https://doi.org/10.1016/j.apsusc.2020.145597

Xu, J., Pan, Q., Shun, Y., & Tian, Z. (2000). Grain size control and gas sensing properties of ZnO gas sensor. *Sensors and Actuators. B, Chemical*, 66(1-3), 277-279. https://doi.org/10.1016/s0925-4005(00)00381-6

Xu, L., Li, X., & Yuan, J. (2008). Effect of K-doping on structural and optical properties of ZnO thin films. *Superlattices and Microstructures*, 44(3), 276-281. https://doi.org/10.1016/j.spmi.2008.04.004

Yang, X., Tian, J., Guo, Y., Teng, M., Liu, H., Li, T., Lv, P., & Wang, X. (2021). ZnO nano-rod arrays synthesized with exposed {0001} facets and the investigation of photocatalytic activity. *Crystals*, 11(5), Article 522. https://doi.org/10.3390/cryst11050522

Yang, J., Wang, J., Li, X., Lang, J., Liu, F., Yang, L., Zhai, H., Gao, M., & Zhao, X. (2012). Effect of polar and non-polar surfaces of ZnO nanostructures on photocatalytic properties. *Journal of Alloys and Compounds*, 528, 28-33. https://doi.org/10.1016/j.jallcom.2012.02.162

Zegadi, C., Abdelkebir, K., Chaumont, D., Adnane, M., & Hamzaoui, S. (2014). Influence of Sn low doping on the morphological, structural and optical properties of ZnO films deposited by sol gel dip-coating. *Advances in Materials Physics and Chemistry*, 4(5), 93-104. https://doi.org/10.4236/ampc.2014.45012

Zhang, M., Averseng, F., Haque, F., Borghetti, P., Krafft, J.-M., Baptiste, B., Costentin, G., & Stankic, S. (2019). Defect-related multicolour emissions in ZnO smoke: from violet, over green to yellow. *Nanoscale*, 11(11), 5102-5115. https://doi.org/10.1039/c8nr09998g

Zhang, Q., Xu, M., You, B., Zhang, Q., Yuan, H., & Ostrikov, K. (2018). Oxygen vacancy-mediated ZnO nanoparticle photocatalyst for degradation of methylene blue. *Applied Sciences*, 8(3), Article 353. https://doi.org/10.3390/app8030353

Zou, X., Ke, J., Hao, J., Yan, X., & Tian, Y. (2022). A new method for synthesis of ZnO flower-like nanostructures and their photocatalytic performance. *Physica. B, Condensed Matter*, 624, Article 413395. https://doi.org/10.1016/j.physb.2021.413395